

Article

# WO<sub>3</sub> Nanoplates Decorated with Au and SnO<sub>2</sub> Nanoparticles for Real-Time Detection of Foodborne Pathogens

Xueyan Li<sup>1</sup>, Zeyi Wu<sup>1</sup>, Xiangyu Song<sup>1</sup>, Denghua Li<sup>2,\*</sup>, Jiajia Liu<sup>1,\*</sup> and Jiatao Zhang<sup>1,3,4</sup>

<sup>1</sup> School of Materials Science and Engineering, Beijing Key Laboratory of Construction-Tailorable Advanced Functional Materials and Green Applications, Beijing Institute of Technology, Beijing 100081, China; zhangjt@bit.edu.cn (J.Z.)

<sup>2</sup> Key Laboratory of Agricultural Information Service Technology of Ministry of Agriculture, Agricultural Information Institute of Chinese Academy of Agricultural Sciences, Beijing 100081, China

<sup>3</sup> School of Chemistry and Chemical Engineering, MIIT Key Laboratory of Medical Molecule Science and Pharmaceutical Engineering, Beijing Institute of Technology, Beijing 100081, China

<sup>4</sup> MOE Key Laboratory of Cluster Science, Beijing Institute of Technology, Beijing 100081, China

\* Correspondence: lidenghua@caas.cn (D.L.); liujiajia@bit.edu.cn (J.L.)

**Abstract:** Nowadays, metal oxide semiconductor gas sensors have diverse applications ranging from human health to smart agriculture with the development of Internet of Things (IoT) technologies. However, high operating temperatures and an unsatisfactory detection capability (high sensitivity, fast response/recovery speed, etc.) hinder their integration into the IoT. Herein, a ternary heterostructure was prepared by decorating WO<sub>3</sub> nanoplates with Au and SnO<sub>2</sub> nanoparticles through a facial photochemical deposition method. This was employed as a sensing material for 3-hydroxy-2-butanone (3H-2B), a biomarker of *Listeria monocytogenes*. These Au/SnO<sub>2</sub>-WO<sub>3</sub> nanoplate-based sensors exhibited an excellent response ( $R_a/R_g = 662$ ) to 25 ppm 3H-2B, which was 24 times higher than that of pure WO<sub>3</sub> nanoplates at 140 °C. Moreover, the 3H-2B sensor showed an ultrafast response and recovery speed to 25 ppm 3H-2B as well as high selectivity. These excellent sensing performances could be attributed to the rich Au/SnO<sub>2</sub>-WO<sub>3</sub> active interfaces and the excellent transport of carriers in nanoplates. Furthermore, a wireless portable gas sensor equipped with the Au/SnO<sub>2</sub>-WO<sub>3</sub> nanoplates was assembled, which was tested using 3H-2B with known concentrations to study the possibilities of real-time gas monitoring in food quality and safety.



**Citation:** Li, X.; Wu, Z.; Song, X.; Li, D.; Liu, J.; Zhang, J. WO<sub>3</sub> Nanoplates Decorated with Au and SnO<sub>2</sub> Nanoparticles for Real-Time Detection of Foodborne Pathogens.

*Nanomaterials* **2024**, *14*, 719. <https://doi.org/10.3390/nano14080719>

Academic Editor: Antonino Gulino

Received: 25 March 2024

Revised: 9 April 2024

Accepted: 15 April 2024

Published: 19 April 2024



**Copyright:** © 2024 by the authors. Licensee MDPI, Basel, Switzerland. This article is an open access article distributed under the terms and conditions of the Creative Commons Attribution (CC BY) license (<https://creativecommons.org/licenses/by/4.0/>).

**Keywords:** Au/SnO<sub>2</sub>-WO<sub>3</sub> nanoplates; photochemical deposition; 3-hydroxy-2-butanone

## 1. Introduction

With the development of Internet of Things (IoT) technologies, gas sensors are in great demand for numerous applications, including food, medical (diagnosis), industry, environment, and agriculture [1,2]. To be integrated into the IoT, there is a strong need for advanced miniature gas sensors with a low cost, low power consumption, and excellent detection capabilities (high sensitivity, fast and sensitive response, etc.) to satisfy the demands of real-time monitoring [3]. Among the various gas sensors, metal oxide semiconductor (MOS)-based chemical-resistive gas sensors are being studied most actively due to their good stability, low cost, compact size, and high sensitivity, which make them a promising candidate for integration into the IoT [4]. However, their high operating temperature (above 300 °C) limits their utilization in the IoT.

Among the various MOSs, attention to tungsten oxide (WO<sub>3</sub>) has increased because its sensing performance mainly depends on the synthesis route, through which the sensing factors (active sites, microstructure, localized gas–solid interface, and so on) can be controlled [5–8]. Moreover, its crystalline lattice allows it to accommodate certain oxygen deficiencies, which could enhance its sensing performance by modulating the electronic

band structure and increasing the carrier densities [9]. However, a single-component  $\text{WO}_3$ -based sensing layer could hardly satisfy all requirements for sensitivity, selectivity, stability, and working temperatures. Diverse strategies, mainly consisting of morphology modulation [4], the construction of heterostructures [10,11], and the decoration of catalysts [6,12], have been developed to improve the gas-sensing capability of  $\text{WO}_3$  nanomaterials. Constructing composite materials has been put forward to create more gas adsorption sites and reduce the charge transport channel, thus enhancing the overall sensing performance. For example, Kaur et al. reported a selective sensing behavior toward both oxidizing and reducing gas analytes by employing  $\text{NiO}/\text{NiWO}_4/\text{WO}_3$  heterojunctions [10]. In addition, decorating MOSs with noble metals (Ag, Au, Pd, and Pt) has been proposed as an effective method to promote the sensing performance at lower operating temperatures [13–16]. For instance,  $\text{WO}_3$  nanoflowers decorated with PtAu bimetallic nanocrystals led to a high response to 20 ppm n-pentanol at 200 °C, a response that was 105 times higher than that for pure  $\text{WO}_3$  [14]. As reported for Pt-anchored  $\text{WO}_3$  chemiresistors, the formation of surface-active sites and inward diffusion induced by a pulse temperature modulation strategy explained the superior response to trimethylamine and xylene [12]. More recently, Zhang et al. prepared Pd/Si-m $\text{WO}_3$  microspheres, which exhibited good selectivity and sensitivity to hydrogen at 210 °C [6]. In addition to these classical heterojunctions built from two components, the construction of heterostructures by assembling different active components offers additional possibilities [17,18]. For example, Tammanoon et al. reported that PdOx–CuOx co-loaded porous  $\text{WO}_3$  microspheres were highly selective and sensitive to methyl mercaptan at 200 °C and, more importantly, the co-loading of PdOx with CuOx significantly improved the methyl mercaptan selectivity against hydrogen sulfide [19]. Overall, the unique heterointerface effect optimizes adsorption/reaction processes and the following charge transfer between the target gas and the sensing layer, thereby decreasing the working temperature and improving the sensing sensitivity. Despite the significant results that have been attained, it is still highly desirable to synthesize  $\text{WO}_3$  hybrid nanocomposites with fine-tuned surface/interface properties to meet future IoT environment monitoring demand.

*Listeria monocytogenes* is a highly contagious foodborne pathogen that causes listeriosis outbreaks primarily in immunocompromised individuals [13]. It can be found in various food sources such as vegetables, meat, seafood, and dairy products and has the ability to survive and even grow under refrigeration and other food preservation measures [20]. Infection from *Listeria monocytogenes* can lead to symptoms such as fever, nausea, diarrhea, and, in severe cases, bacteremia, complications, and meningitis [20]. According to the World Health Organization (WHO), although listeriosis is a relatively rare disease (with 0.1 to 10 cases per 1 million people per year, depending on geographical location), its high fatality rate makes it a significant public health concern [21]. For instance, a listeriosis outbreak in South Africa in 2018 resulted in 1024 infections and over 200 deaths [22], while another outbreak associated with enoki mushrooms affected 48 individuals in 2020 [23]. Conventional methods such as plate colony counts, biochemical tests, molecular assays, and immunoassays require professional operators and specialized equipment, and it requires a few days to a week to obtain results [24]. Therefore, there is an urgent need for the development of rapid, effective, and user-friendly techniques to detect *Listeria monocytogenes*. Recently, the detection of specific microbial volatile organic compounds (WVOCs) has emerged as a promising method for on-site pathogen detection and identification [25]. Among the WVOCs of *Listeria monocytogenes*, one is 3-hydroxy-2-butanone (3H-2B), which accounts for approximately a 32% abundance. Moreover, the concentration of 3H-2B exhibits a good linear relation with the incubation time of *Listeria monocytogenes* [26]. Since the initial exploration by Zhu et al., who investigated the feasibility of utilizing mesoporous  $\text{WO}_3$  nanomaterials for the selective detection of 3H-2B to monitor *Listeria monocytogenes*, various MOS nanomaterials with diverse morphologies have been employed to detect 3H-2B [26]. For instance, mesoporous  $\text{WO}_3/\text{Au}$  nanocomposites prepared using a soft-template approach demonstrated a sensitive detection of 3H-2B (175 °C;  $R_a/R_g = 18.8$  to

2.5 ppm) [27]. Zeb et al. synthesized AuPdO-modified Cu-doped  $K_2W_4O_{13}$  nanowires via hydrothermal treatments, followed by in situ reduction and impregnation, which exhibited dual selectivity in detecting 3H-2B at 120 °C ( $R_a/R_g = 242$  to 10 ppm) and triethylamine at 200 °C, respectively [28]. Wang et al. developed a highly sensitive 3H-2B sensor based on zinc oxide nanorods decorated with  $Co_3O_4$  nanoparticles, delivering an exceptional sensing performance (260 °C;  $R_a/R_g = 550$  to 5 ppm) [29]. However, these aforementioned nanomaterials still possess limitations in terms of their material synthetic complexity, response/recovery time, sensitivity, limit of detection, and selectivity, thus necessitating further efforts toward the development of more sensitive sensing materials with a facile synthesis method for the real-time tracing of *Listeria monocytogenes*.

Herein, a ternary heterostructure was prepared by decorating  $WO_3$  nanoplates with Au and  $SnO_2$  nanoparticles through a facial photochemical deposition method. These nanocomposite materials were carefully characterized in terms of morphology and structure and their gas sensitivities to 3H-2B were measured. The underlying sensing mechanisms were discussed. Furthermore, a portable gas sensor loaded with the Au/ $SnO_2$ - $WO_3$  nanoplates was assembled, which was tested using 3H-2B with known concentrations to study the possibilities of real-time gas monitoring in food quality and safety.

## 2. Materials and Methods

The  $WO_3$  nanoplates were prepared via the hydrothermal and calcination method. Typically, 300 mg sodium tungstate (Sinopharm, Shanghai, China) was added to 15 mL deionized water and stirred for 10 min. Then, 0.45 mL L-lactic acid (Aladdin, Shanghai, China) and 0.675 mL of a 6 mol/L hydrochloric acid (Tgreag, Beijing, China) solution were added in order, with stirring after each addition. The resulting solution was heated at 120 °C for 12 h and a yellow-green powder was collected after washing and drying. Finally, the  $WO_3$  nanoplates were produced after calcination under an air atmosphere at 500 °C for 1 h. The deposition of Au or  $SnO_2$  nanoparticles on the surface of the  $WO_3$  nanoplates was carried out using the photochemical deposition method. Typically, 50 mg  $WO_3$  was dispersed in 40 mL deionized water. The mixture was stirred for 10 min and then we added X (X = 0.5, 0.75, 1, and 1.25) mL  $H AuCl_4$  (5 mg/mL) (Sinopharm, Shanghai, China) and  $SnCl_2$  (5 mg/mL) (Aladdin, Shanghai, China). Under continuous stirring and Xenon lamp irradiation for 4 h, a purple suspension was obtained. The purple suspension was centrifuged, washed, and dried to obtain purple powder samples, designated as XAu/ $SnO_2$ - $WO_3$  nanoplates. For comparison, Au- $WO_3$  and  $SnO_2$ - $WO_3$  nanoplates were also prepared under the same deposition conditions from  $H AuCl_4$  or  $SnCl_2$  and  $KIO_3$  on the surface of  $WO_3$  nanoplates, respectively. The prepared samples are summarized in Table S1. Characterizations for all samples are shown in the Supplementary Materials.

A gas-response instrument (WS-30B, Weisheng Ltd., Zhengzhou, China) was used to measure the gas-sensing characteristics using the static gas distribution method. The procedure for the sensing film preparation and gas-sensing measurements is described in detail in the Supplementary Materials. The resistance ratio between the gas sensor in air ( $R_a$ ) and the target gas ( $R_g$ ) was calculated as the gas response, where  $R_g/R_a$  and  $R_a/R_g$  were the oxidizing gas and reducing gases, respectively. The response/recovery time was defined as the time for the variation in the gas response to reach 90% of the equilibrium value after a test gas was injected or released.

## 3. Results and Discussion

### 3.1. Morphology of $WO_3$ , $SnO_2$ - $WO_3$ , and XAu/ $SnO_2$ - $WO_3$ Nanoplates

The procedure for the synthesis of the XAu/ $SnO_2$ - $WO_3$  nanoplates is illustrated in Figure 1a. The  $WO_3$  nanoplates were initially synthesized using the hydrothermal and calcination method. As shown in Figure S1,  $WO_3 \cdot H_2O$  nanoplates were generated after a hydrothermal treatment. Samples calcinated at different temperature were characterized using TEM (Hitachi H-7650, Hitachi, Japan) and XRD (Bruker D8, Karlsruhe, German) techniques (Figure S2), and monoclinic  $WO_3$  nanoplates with a uniform size (200~300 nm)

were selected for further modification. Finally, the Au and SnO<sub>2</sub> nanoparticles were decorated on the WO<sub>3</sub> nanoplates using the photochemical deposition method. Photochemical deposition is an effective method for co-catalyst deposition in the synthesis of photocatalysts, involving reductive and oxidative photodeposition by photogenerated electrons and photoinduced holes, respectively [30]. Generally, sacrificial electron donors/acceptors are required during reductive/oxidative photodeposition. Herein, Au and SnO<sub>2</sub> nanoparticles were simultaneously photochemically deposited onto WO<sub>3</sub> nanoplates using HAuCl<sub>4</sub> and SnCl<sub>2</sub> solutions as precursors. The morphology and structural observation of the obtained samples are shown in Figures 1b and S3. The large dark spots on the WO<sub>3</sub> nanoplates were believed to be Au nanoparticles, while the light chain-like nanoparticles were SnO<sub>2</sub> nanoparticles (Figure S3). The HRTEM image in Figure 1c demonstrates that the Au and SnO<sub>2</sub> nanoparticles were effectively decorated onto the WO<sub>3</sub> nanoplates. The lattice spacings of 0.39 nm, 0.22 nm, and 0.26 nm matched well with the (002) crystal plane of WO<sub>3</sub>, the (111) plane of Au, and the (101) plane of SnO<sub>2</sub>, respectively, where the formation of heterogeneous interfaces resulted in a slight lattice distortion. The high-angle annular dark-field scanning TEM (HAADF-STEM) image and corresponding energy-dispersive X-ray spectroscopy (EDS) elemental mapping (Figure 1d) confirmed the homogeneous distribution of Au and Sn elements in the XAu/SnO<sub>2</sub>-WO<sub>3</sub> nanoplates. Some large Au nanoparticles were found, similar to the samples obtained using the photochemical deposition method [31]. These results demonstrated the formation of XAu/SnO<sub>2</sub>-WO<sub>3</sub> composites with an intensely coupled interaction between the individual components.

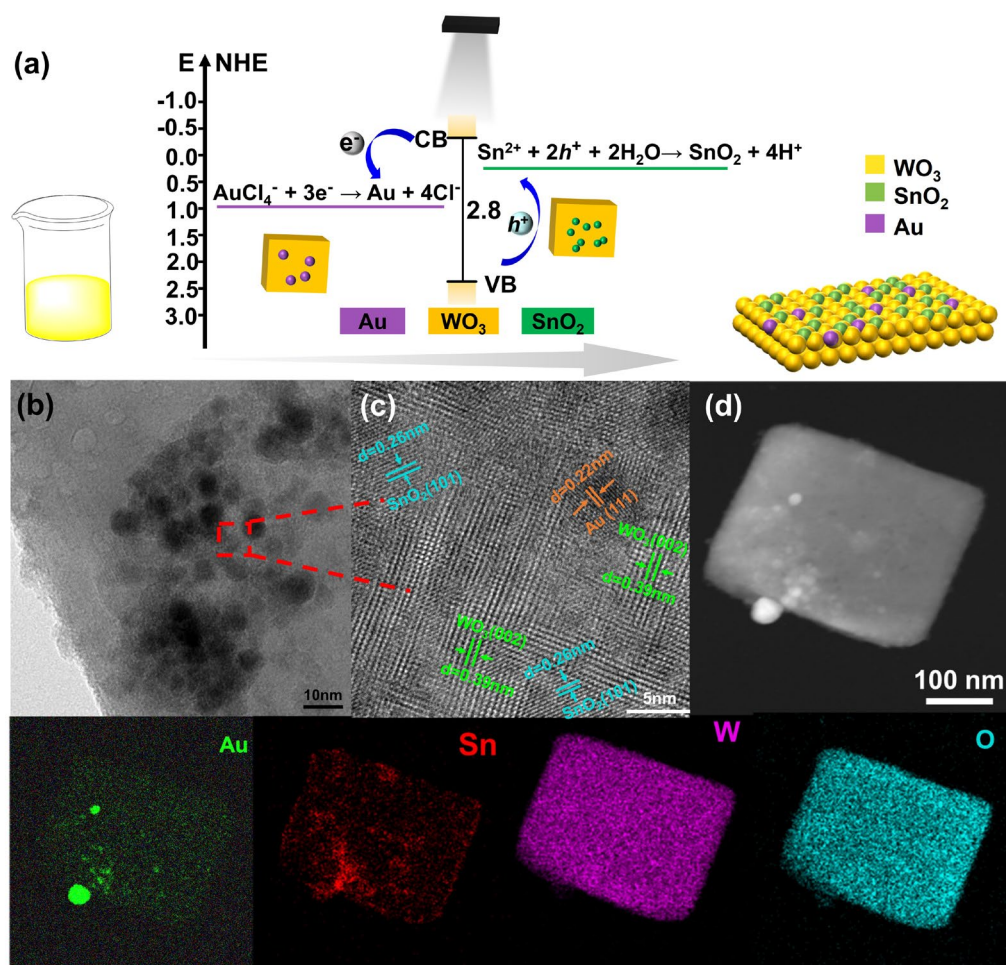


**Figure 1.** (a) The synthesis schematic of XAu/SnO<sub>2</sub>-WO<sub>3</sub> nanoplates. (b,c) HRTEM images. (d) HAADF-STEM image and corresponding EDS elemental mapping results of the 1Au/SnO<sub>2</sub>-WO<sub>3</sub> nanoplates.

### 3.2. Microstructure of $\text{WO}_3$ , $\text{SnO}_2\text{-WO}_3$ , and $\text{XAu/SnO}_2\text{-WO}_3$ Nanoplates

An XRD analysis was carried out to characterize the crystal structures of the as-prepared samples. As shown in Figures 2a and S4a, the diffraction peaks of all the samples matched well with the monoclinic crystal structure of  $\text{WO}_3$  (JCPDS No. 83-0950). The characteristic peak of  $\text{SnO}_2$  at  $33.887^\circ$  only appeared in  $\text{SnO}_2\text{-WO}_3$ , corresponding with the (101) crystal plane of  $\text{SnO}_2$  (JCPDS No. 72-1147). For  $\text{Au-WO}_3$ , the characteristic peak appeared at  $38.184^\circ$ , corresponding with the (111) crystal plane of Au (JCPDS No. 04-0784). However, there was no characteristic peaks of Au and  $\text{SnO}_2$  detected in the  $\text{XAu/SnO}_2\text{-WO}_3$  nanoplates, which could be ascribed to the small loading amount of Au and  $\text{SnO}_2$ .

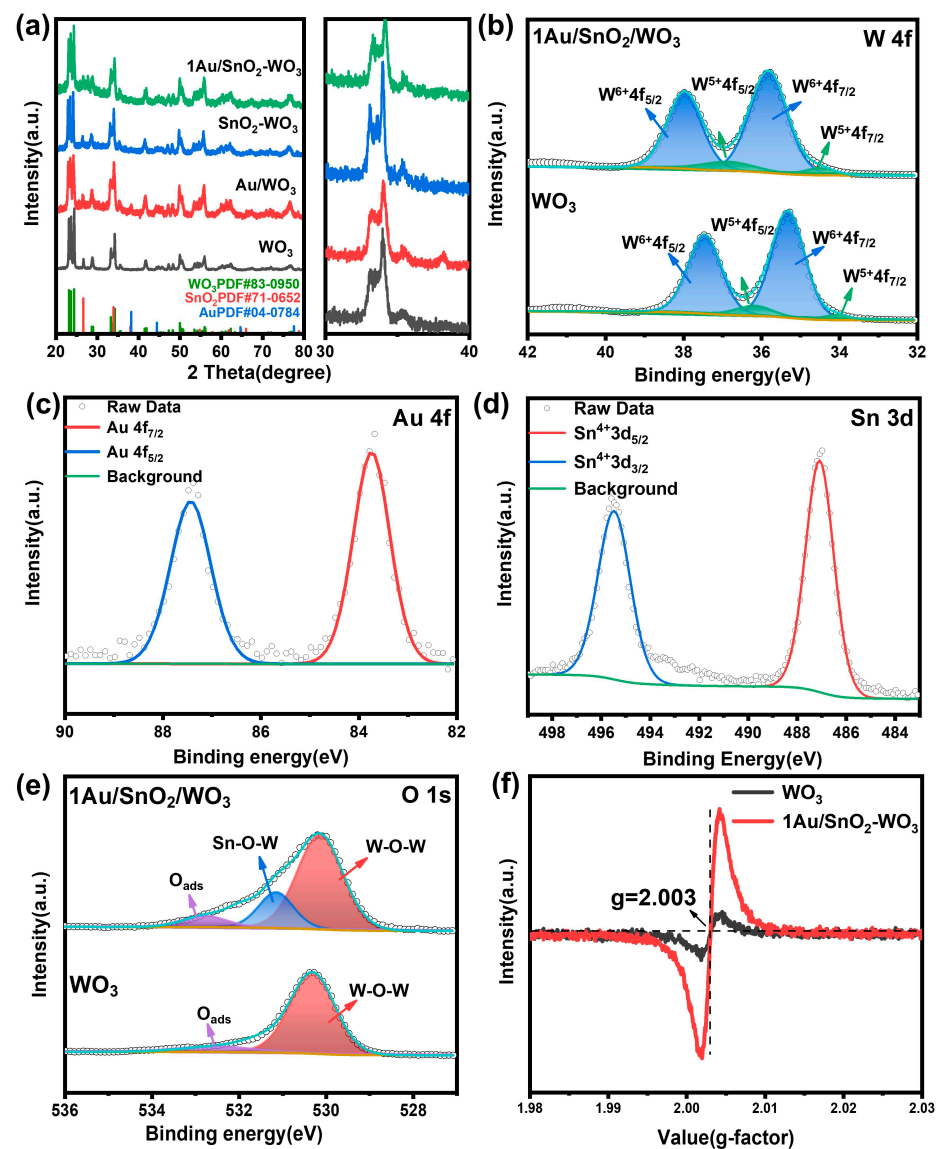


**Figure 2.** (a) XRD patterns of  $\text{WO}_3$  nanoplates,  $\text{Au-WO}_3$  nanoplates,  $\text{SnO}_2\text{-WO}_3$  nanoplates, and  $\text{1Au/SnO}_2\text{-WO}_3$  nanoplates; XPS spectra of (b) W 4f, (c) Au 4f, (d) Sn 3d, and (e) O 1s; (f) EPR spectra of  $\text{WO}_3$  and  $\text{1Au/SnO}_2\text{-WO}_3$  nanoplates.

X-ray photoelectron spectroscopy (XPS) measurements were used to further analyze the chemical state of the elements (Figures 2b–e and S4b,c). The survey spectrum (Figure S4b) demonstrated the presence of W, Sn, Au, and O, indicating the high purity of the samples. Figure 2b compares the spectra of W 4f in  $\text{WO}_3$  and the  $\text{1Au/SnO}_2\text{-WO}_3$  nanoplates. The peaks of  $\text{W}^{6+}$  (35.81 eV and 37.7 eV) and  $\text{W}^{5+}$  (34.5 eV and 36.5 eV) shifted

toward the high binding energy side. This indicated that there was a strong interaction between  $\text{WO}_3$ , Au, and  $\text{SnO}_2$  and the electrons around the W atom decreased [32]. In the 4f spectrum of the Au element, the peaks at the binding energies of 83.86 eV and 87.54 eV matched well with Au 4f<sub>7/2</sub> and Au 4f<sub>5/2</sub>, indicating that the Au element existed in the form of Au [33,34]. In the 3d spectrum of the Sn element, the peaks at the binding energies of 487.18 eV and 495.56 eV corresponded with Sn 3d<sub>5/2</sub> and Sn 3d<sub>3/2</sub>, respectively, indicating that Sn existed in a +4 oxidation state [35]. The mass percentage of the Au and Sn elements is listed in Table S2. With an increase in the dosage, the content of the Au and Sn elements in the sample also increased. The O 1s XPS spectra of the  $\text{WO}_3$  and 1Au/ $\text{SnO}_2$ - $\text{WO}_3$  nanoplates (Figure 2e) could be deconvoluted into different peaks, corresponding with W-O-W (530.1 eV) [36], Sn-O-W (531.94 eV) [37], and adsorbed oxygen ( $\text{O}_{\text{ads}}$ ; 532.58 eV), respectively. The proportion of adsorbed O increased in the 1Au/ $\text{SnO}_2$ - $\text{WO}_3$  nanoplates, which could be ascribed to surface oxygen vacancies. The appearance of the Sn-O-W bond indicated that there was a good interfacial interaction between the  $\text{SnO}_2$  and  $\text{WO}_3$  phases.

An electron paramagnetic resonance (EPR) (Bruker A300-10/12, German) analysis was carried out to study the surface oxygen vacancies of the samples. As shown in Figure 2f, there was a relatively higher intensity peak at  $g \approx 2.003$  for the 1Au/ $\text{SnO}_2$ - $\text{WO}_3$  nanoplates than that of the  $\text{WO}_3$  nanoplates under the same conditions, indicating electron trapping at oxygen vacancies [38]. These results confirmed the presence of surface oxygen vacancies on the 1Au/ $\text{SnO}_2$ - $\text{WO}_3$  nanoplates, which correlated with the above XPS results. Figure S4d shows the Raman spectra of the  $\text{WO}_3$  and 1Au/ $\text{SnO}_2$ - $\text{WO}_3$  nanoplates. As the W-O bond changed due to the increase in oxygen vacancy, the peak of the 1Au/ $\text{SnO}_2$ - $\text{WO}_3$  nanoplates moved to a longer wavelength at  $600 \text{ cm}^{-1}$  and the peak intensity became weaker than that of the  $\text{WO}_3$  nanoplates.

### 3.3. Gas-Sensing Performance

The gas-sensing performance of the as-prepared samples was carefully studied and compared. Given that the operating temperature strongly affects sensing performances, the optimum working temperatures of the sensors were first identified. As shown in Figure 3a, sensors based on the  $\text{WO}_3$ , Au- $\text{WO}_3$ ,  $\text{SnO}_2$ - $\text{WO}_3$ , and XAu/ $\text{SnO}_2$ - $\text{WO}_3$  nanoplates exhibited a notable response in a 25 ppm 3-hydroxy-2-butanone (3H-2B, 98%; Aladdin, Shanghai, China) atmosphere within an operating temperature range of 80–180 °C. The response patterns of all the sensors displayed a similar trend of increasing before decreasing. Notably, the sensing response values of the XAu/ $\text{SnO}_2$ - $\text{WO}_3$  nanoplates to 25 ppm 3H-2B at 140 °C were significantly higher than those of the  $\text{WO}_3$ , Au- $\text{WO}_3$ , and  $\text{SnO}_2$ - $\text{WO}_3$  sensors. Among them, the 1Au/ $\text{SnO}_2$ - $\text{WO}_3$  nanoplates showed the maximum response of 662 to 25 ppm 3H-2B at 140 °C, which was 24 times larger than that of the  $\text{WO}_3$  sensor. The working temperature was selected as 140 °C for the subsequent tests. With an increase in the deposition amount of Au and  $\text{SnO}_2$ , the sensing response to the target gas increased, but the response value of 1.25Au/ $\text{SnO}_2$ - $\text{WO}_3$  to 3H-2B began to decrease due to the aggregation and growth of Au and  $\text{SnO}_2$  nanoparticles and the reduction in active sites. The detectivity of all the sensors toward 1.25–25 ppm 3H-2B was further tested (Figure 3b), which was transformed into a dot-line plot (Figure 3c). The 1Au/ $\text{SnO}_2$ - $\text{WO}_3$  nanoplate-based sensors exhibited an enhanced response for the whole detection range, indicating a good linear relationship. In terms of the sensing speed, the 1Au/ $\text{SnO}_2$ - $\text{WO}_3$  nanoplates showed a short response/recovery time of 25s and 11s, respectively (Figure 3d). Moreover, the 1Au/ $\text{SnO}_2$ - $\text{WO}_3$  nanoplate-based sensors exhibited a quick response and could repeatedly be tested when cycled between 3H-2B gas and ambient air (Figure S5), indicating good reproducibility. The 1Au/ $\text{SnO}_2$ - $\text{WO}_3$  nanoplate sensor had a higher baseline resistance, about 16 times higher than that of the  $\text{WO}_3$  sensor (Figure 3e). The high baseline resistance may have originated from the existence of a large amount of oxygen on the surface of the 1Au/ $\text{SnO}_2$ - $\text{WO}_3$  nanoplates.

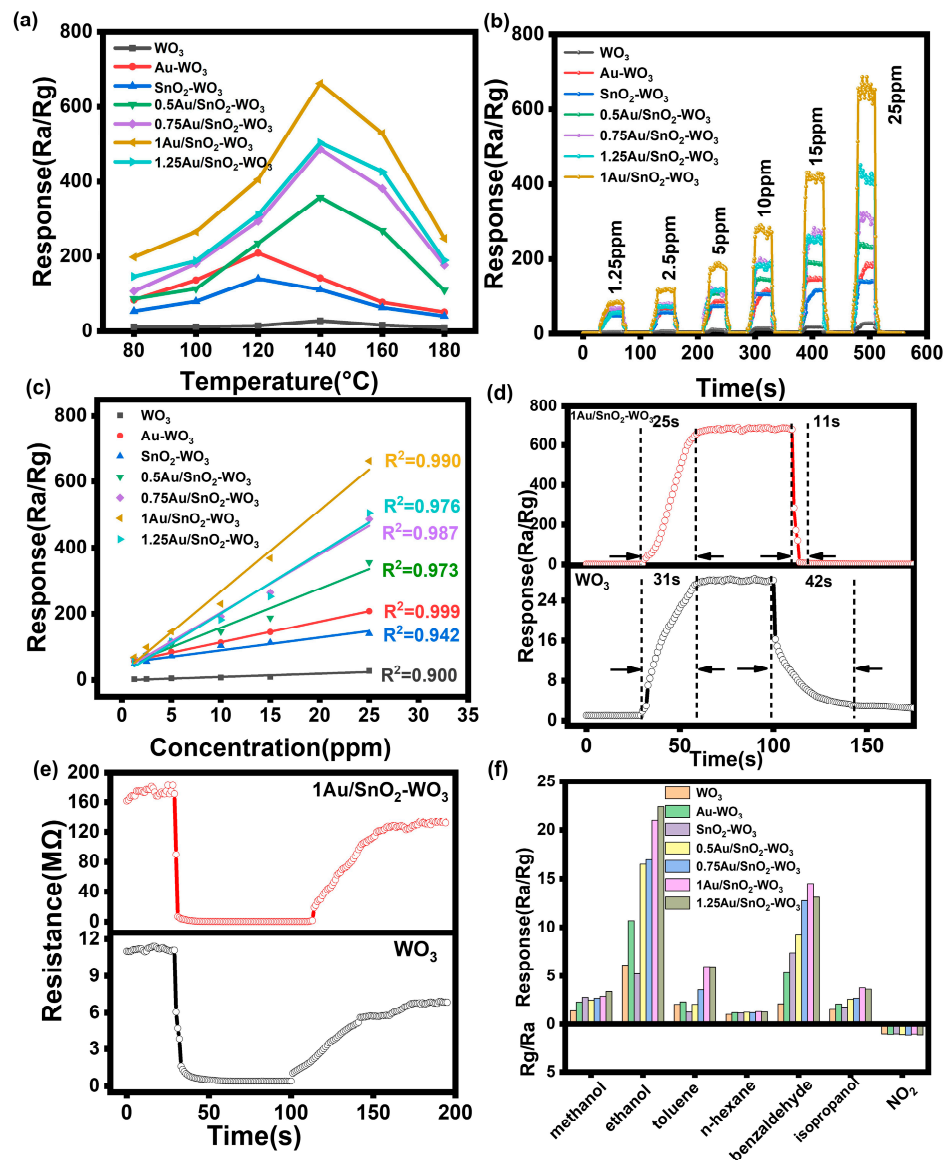


**Figure 3.** (a) Response curves of  $\text{WO}_3$  and  $\text{XAu/SnO}_2\text{-WO}_3$  nanoplatform-based sensors to 25 ppm 3H-2B at different working temperatures. (b) Dynamic response and recovery curves of  $\text{WO}_3$  and  $\text{XAu/SnO}_2\text{-WO}_3$  nanoplatform-based sensors toward different concentrations (1.25, 2.5, 5, 10, 15, and 25 ppm) of 3H-2B at 140 °C. (c) Response curves of  $\text{WO}_3$  and  $\text{XAu/SnO}_2\text{-WO}_3$  nanoplatform-based sensors toward different concentrations of 3H-2B. (d,e) Dynamic response and recovery curves of  $\text{WO}_3$  and  $\text{XAu/SnO}_2\text{-WO}_3$  nanoplatform-based sensors toward 25 ppm 3H-2B. (f) Selectivity tests of  $\text{WO}_3$  and  $\text{XAu/SnO}_2\text{-WO}_3$  nanoplatform-based sensors toward different target gases.

Other than sensitivity and rapid response/recovery, selectivity is another important factor in practical applications. The sensors were tested using different interference gases (methanol, ethanol, toluene, n-hexane, benzaldehyde, isopropyl alcohol, acetone, ammonia, formaldehyde, and  $\text{NO}_2$ ) at 25 ppm at 140 °C. At a low working temperature (140 °C), no valid detection value could be obtained for acetone, ammonia, and formaldehyde. *Listeria monocytogenes* is a contagious food pathogen that exists in vegetables, fish, meat, and dairy products, causing fatal foodborne illness. 3-Hydroxy-2-butanone (32.2% abundance) and benzaldehyde (17.6% abundance) are the typical microbial volatile organic compounds produced by *Listeria monocytogenes*, which can be characterized as biomarkers [27]. The response of all sensors to 3H-2B was higher than that for other gases (Figure 3f). Among them, the response of the 1Au/ $\text{SnO}_2\text{-WO}_3$  nanoplatform sensors to 3H-2B was the highest

and was 45.98 times that of benzaldehyde and 185 times that of methanol. The response to oxidizing gas  $\text{NO}_2$  could be ignored. The detection results of 3H-2B using different MOS-based sensors in recent years are summarized in Table 1. Accordingly, the 1Au/SnO<sub>2</sub>-WO<sub>3</sub> nanoplate sensors used in the present study exhibited a highly sensitive, good selective, and rapid detection of 3H-2B at a low temperature, which is beneficial for the convenient detection of *Listeria monocytogenes*.

**Table 1.** Comparison of the gas-sensing performance of MOS-based sensors to 3H-2B.

Sensing Materials	T (°C)	$\tau_{res}/\tau_{recov}$ (s)	3H-2B (ppm)	Response ( $R_a/R_g$ )	LOD (ppm)	Ref.
WO <sub>3</sub>	205	25/146	25	152	0.4	[39]
ZnO@Al <sub>2</sub> O <sub>3</sub>	300	27/34	50	37.2	10	[40]
Cr <sub>2</sub> O <sub>3</sub> /SnO <sub>2</sub>	240	9/4	50	280	0.02	[41]
Pt-doped SnO <sub>2</sub>	250	11/20	10	48.69	0.5	[42]
Pd-BiVO <sub>4</sub>	200	12/8	10	103.7	0.2	[43]
M-NiO NCs	120	49/52	50	302	0.5	[44]
WO <sub>3</sub> /Au	175	15/45	2.5	18.8	2.5	[26]
1Au/SnO <sub>2</sub> -WO <sub>3</sub>	140	25/11	25	662	1.25	This work

### 3.4. Sensing Mechanism

The 3H-2B-sensing mechanism of WO<sub>3</sub>-based sensors has been investigated in previous reports [26,27]. As illustrated in Figure 4, when n-type WO<sub>3</sub> was exposed to air, an electron depletion layer was formed on the surface of WO<sub>3</sub> due to the adsorption of oxygen molecules. Thereafter, when 3H-2B was introduced, the target gas reacted with the chemisorbed oxygen species, producing byproducts of acetic acid, 2,3-butanedione, and eventually H<sub>2</sub>O and CO<sub>2</sub>. Thus, this reaction process released the captured electrons and shortened the electron depletion layer, decreasing the resistance. The improved 3H-2B-sensing performance of the 1Au/SnO<sub>2</sub>-WO<sub>3</sub> nanoplates could be ascribed to (i) the heterojunctions between the Au and SnO<sub>2</sub> nanoparticles and the WO<sub>3</sub> nanoplates, (ii) the spillover effect of catalytic Au nanoparticles, and (iii) sufficient oxygen vacancies. First of all, the differences in the work function of dominant WO<sub>3</sub> (5.24 eV) and partially dispersed SnO<sub>2</sub> (4.9 eV) formed an additional electron depletion layer, inducing an increase in the material resistance [45]. In addition, the introduction of Au nanoparticles remarkably improved the dissociation of oxygen molecules, resulting in the further expansion of the electron depletion layer. This was consistent with the observed differentiation in bulk resistance, where the base resistance of the 1Au/SnO<sub>2</sub>-WO<sub>3</sub> nanoplates (180 MΩ) was larger than that of the WO<sub>3</sub> nanoplates (11 MΩ) (Figure 3e). Furthermore, there were more active sites for the adsorption and oxidation of 3H-2B due to the presence of oxygen vacancies. The changes in the work function values, Fermi level, and band edge position for the 1Au/SnO<sub>2</sub>-WO<sub>3</sub> nanoplates were determined using UV-vis absorption spectroscopy and ultraviolet photoelectron spectroscopy (Figure S6). The determined work functions stood at 4.77 and 4.39 eV respectively, pertaining to the WO<sub>3</sub> and 1Au/SnO<sub>2</sub>-WO<sub>3</sub> nanoplates. The disparity in the work functions suggested a higher electron population in the conduction band of the 1Au/SnO<sub>2</sub>-WO<sub>3</sub> nanoplates compared with that of the WO<sub>3</sub> nanoplates, thereby augmenting the adsorption capacity for oxygen species. Consequently, this facilitated an efficient electron exchange with gas molecules and promoted a more facile gas-sensing process.

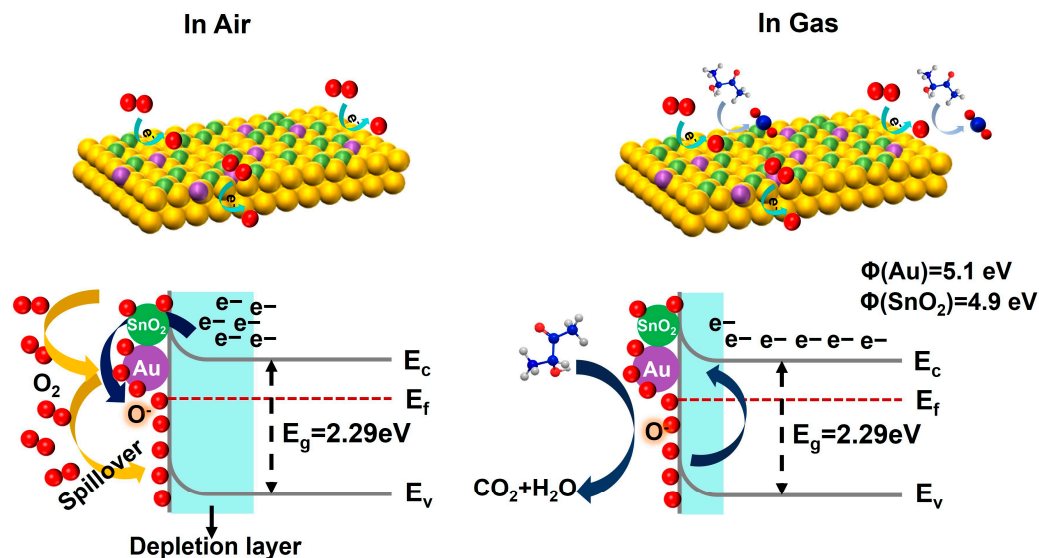


**Figure 4.** Schematic of the surface-sensing reaction of 1Au/SnO<sub>2</sub>-WO<sub>3</sub> nanoplates toward 3H-2B and the corresponding band diagram of the sensing mechanism.

### 3.5. Wireless Portable Sensor

In order to realize the real-time detection of 3H-2B, a wireless portable sensor based on the 1Au/SnO<sub>2</sub>-WO<sub>3</sub> nanoplate gas sensor was developed and connected to a laptop via ZigBee, which provided the sensing information (Figure 5). By integrating the power module, electric heating wire temperature control module, series resistor selection module, wireless module, main control chip, and sensing module on an 8 cm × 8 cm PCB circuit board using integrated circuit technology, the volume of the gas detection device was significantly reduced, resulting in cost savings and reduced power consumption. The homemade portable sensor displayed a rapid sensing response toward 25 ppm 3H-2B at 140 °C, which was comparable with the sensing information obtained from the gas-response instrument. The feasibility of the on-site monitoring of *Listeria monocytogenes* by detecting the concentration of 3H-2B has been demonstrated [13,46]; thus, these results suggest that a portable gas sensor holds great potential for the rapid identification of foodborne pathogens.

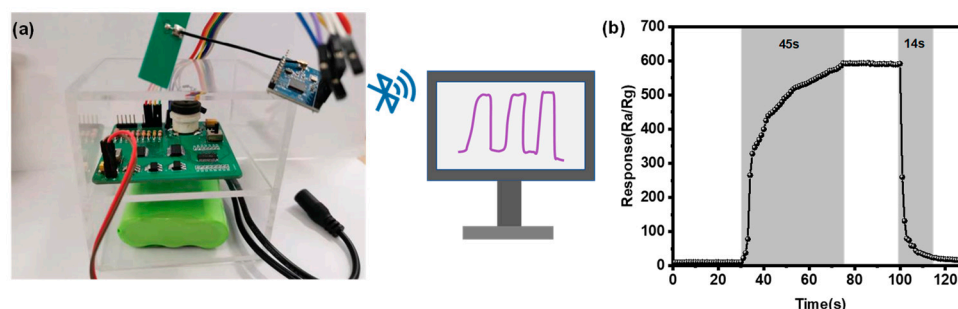


**Figure 5.** (a) Optical photograph of wireless portable sensor connected to a laptop via ZigBee. (b) Dynamic response and recovery curves displayed on the laptop when the portable sensor was exposed to 25 ppm 3H-2B.

## 4. Conclusions

In summary, a ternary heterostructure was prepared by decorating WO<sub>3</sub> nanoplates with Au and SnO<sub>2</sub> nanoparticles through a facial photochemical deposition method, and was employed as a sensing material for 3-hydroxy-2-butanone (3H-2B), a biomarker of *Listeria monocytogenes*. These 1Au/SnO<sub>2</sub>-WO<sub>3</sub> nanoplate-based sensors exhibited an excellent response ( $R_a/R_g = 662$ ) to 25 ppm 3H-2B, which was 24 times higher than that of the pure

WO<sub>3</sub> nanoplates at 140 °C. Moreover, the 3H-2B sensor showed rapid response/recovery and high selectivity. These exceptional sensing performances could be attributed to the heterojunctions between the Au and SnO<sub>2</sub> nanoparticles and the WO<sub>3</sub> nanoplates, the spillover effect of the catalytic Au nanoparticles, and abundant oxygen vacancies. Furthermore, a wireless portable gas sensor equipped with the 1Au/SnO<sub>2</sub>-WO<sub>3</sub> nanoplates was assembled and exhibited comparable detection values with the sensing information obtained from the gas-response instrument.

**Supplementary Materials:** The following supporting information can be downloaded at: <https://www.mdpi.com/article/10.3390/nano14080719/s1>, Figure S1: TEM images and XRD patterns of WO<sub>3</sub>·H<sub>2</sub>O nanosheets; Figure S2: TEM images and XRD patterns of WO<sub>3</sub>·H<sub>2</sub>O nanoplates; Figure S3: TEM images and SEM images of Au-WO<sub>3</sub> nanoplates, SnO<sub>2</sub>-WO<sub>3</sub> nanoplates, and XAu/SnO<sub>2</sub>-WO<sub>3</sub> nanoplates; Figure S4: XRD and XPS patterns of XAu/SnO<sub>2</sub>-WO<sub>3</sub> nanoplates; Figure S5: Dynamic sensing response of the sensor based on 1Au/SnO<sub>2</sub>-WO<sub>3</sub> nanoplates to 25 ppm 3H-2B at 140 °C; Figure S6: UV-vis absorption spectra, Tauc plots, and UPS spectra of WO<sub>3</sub> and 1Au/SnO<sub>2</sub>-WO<sub>3</sub> nanoplates; Table S1: The mass percentage of Au and Sn elements in XAu/SnO<sub>2</sub>-WO<sub>3</sub> nanoplates; Table S2. The mass percentage of Au and Sn elements in XAu/SnO<sub>2</sub>-WO<sub>3</sub> nanoplates. Note S1: Chemicals and Materials, Characterizations, and Gas-Sensing Measurements.

**Author Contributions:** Methodology, validation, formal analysis, and writing—original draft preparation, X.L.; investigation and data curation, X.L., Z.W. and X.S.; conceptualization, visualization, resources, supervision, and project administration, J.L.; writing—review and editing and funding acquisition, D.L. and J.Z. All authors have read and agreed to the published version of the manuscript.

**Funding:** This research was funded by the National Natural Science Foundation of China (Grant Nos. 52272186, 22375020, 52303366, 22105116 and 62105030), Beijing Institute of Technology Research Fund Program for Young Scholars, Open Fund of Key Laboratory of Agricultural Monitoring and Early Warning Technology, Ministry of Agriculture and Rural Affairs (JCYJKFKT2201).

**Data Availability Statement:** Data are contained within the article and Supplementary Materials.

**Acknowledgments:** The authors thank the technical supporting from Analysis & Testing Center, Beijing Institute of Technology.

**Conflicts of Interest:** The authors declare no conflicts of interest.

## References

1. Zhang, H.; Zhang, Z.; Li, Z.; Song, W.; Yi, J. A chemiresistive-potentiometric multivariate sensor for discriminative gas detection. *Nat. Commun.* **2023**, *14*, 3495. [[CrossRef](#)] [[PubMed](#)]
2. Chun, S.Y.; Song, Y.G.; Kim, J.E.; Kwon, J.U.; Soh, K.; Kwon, J.Y.; Kang, C.Y.; Yoon, J.H. An artificial olfactory system based on a chemi-memristive device. *Adv. Mater.* **2023**, *35*, 2302219. [[CrossRef](#)] [[PubMed](#)]
3. Yun, J.; Cho, M.; Lee, K.; Kang, M.; Park, I. A review of nanostructure-based gas sensors in a power consumption perspective. *Sens. Actuators B Chem.* **2022**, *372*, 132612. [[CrossRef](#)]
4. Yang, X.; Deng, Y.; Yang, H.; Liao, Y.; Cheng, X.; Zou, Y.; Wu, L.; Deng, Y. Functionalization of mesoporous semiconductor metal oxides for gas sensing: Recent advances and emerging challenges. *Adv. Sci.* **2022**, *10*, 2204810. [[CrossRef](#)] [[PubMed](#)]
5. Galstyan, V.; Poli, N.; D'Arco, A.; Macis, S.; Lupi, S.; Comini, E. A novel approach for green synthesis of WO<sub>3</sub> nanomaterials and their highly selective chemical sensing properties. *J. Mater. Chem. A* **2020**, *8*, 20373–20385. [[CrossRef](#)]
6. Zhang, Z.; Ma, J.; Deng, Y.; Ren, Y.; Xie, W.; Deng, Y.; Zou, Y.; Luo, W. Polymerization-induced aggregation approach toward uniform Pd nanoparticle-decorated mesoporous SiO<sub>2</sub>/WO<sub>3</sub> microspheres for hydrogen sensing. *ACS Appl. Mater. Interfaces* **2023**, *15*, 15721–15731. [[CrossRef](#)] [[PubMed](#)]
7. Ren, Y.; Zou, Y.; Liu, Y.; Zhou, X.; Ma, J.; Zhao, D.; Wei, G.; Ai, Y.; Xi, S.; Deng, Y. Synthesis of orthogonally assembled 3D cross-stacked metal oxide semiconducting nanowires. *Nat. Mater.* **2020**, *19*, 203–211. [[CrossRef](#)] [[PubMed](#)]
8. Staerz, A.; Somacescu, S.; Epifani, M.; Kida, T.; Weimar, U.; Barsan, N. WO<sub>3</sub>-based gas sensors: Identifying inherent qualities and understanding the sensing mechanism. *ACS Sens.* **2020**, *5*, 1624–1633. [[CrossRef](#)]
9. Zeb, S.; Yang, Z.; Hu, R.; Umair, M.; Naz, S.; Cui, Y.; Qin, C.; Liu, T.; Jiang, X. Electronic structure and oxygen vacancy tuning of Co & Ni co-doped W18O<sub>49</sub> nanourchins for efficient TEA gas sensing. *Chem. Eng. J.* **2023**, *465*, 142815.
10. Kaur, N.; Zappa, D.; Maraloiu, V.A.; Comini, E. Novel christmas branched like NiO/NiWO<sub>4</sub>/WO<sub>3</sub> (p-p-n) nanowire heterostructures for chemical sensing. *Adv. Funct. Mater.* **2021**, *31*, 2104416. [[CrossRef](#)]
11. Liu, D.; Li, X.; Li, Y.; Yin, S.; Liu, J.; Zhang, J. Fe-functionalized alpha-Fe<sub>2</sub>O<sub>3</sub>/ZnO nanocages for ppb-level acetone gas sensing. *ACS Appl. Nano Mater.* **2022**, *5*, 5745–5755. [[CrossRef](#)]

12. Dai, T.; Yan, Z.; Li, M.; Han, Y.; Deng, Z.; Wang, S.; Wang, R.; Xu, X.; Shi, L.; Tong, W.; et al. Boosting electrical response toward trace volatile organic compounds molecules via pulsed temperature modulation of Pt anchored WO<sub>3</sub> chemiresistor. *Small Methods* **2022**, *6*, 2200728. [[CrossRef](#)] [[PubMed](#)]
13. Xie, S.; Zhao, C.; Shen, J.; Wei, J.; Liu, H.; Pan, Y.; Zhao, Y.; Zhu, Y. Hierarchical flower-like WO<sub>3</sub> nanospheres decorated with bimetallic Au and Pd for highly sensitive and selective detection of 3-Hydroxy-2-butanone biomarker. *ACS Sens.* **2023**, *8*, 728–738. [[CrossRef](#)] [[PubMed](#)]
14. Wang, Y.; Li, Y.; Yang, L.; Liu, Z.; Li, Y.; Bai, J.; Liu, F.; Liang, X.; Sun, P.; Lu, G. Fast detection of ppm n-pentanol by PtAu alloy nanocrystals decorated flower-like WO<sub>3</sub>. *Sens. Actuators B Chem.* **2022**, *317*, 132623. [[CrossRef](#)]
15. Zhu, Z.; Xing, X.; Feng, D.; Li, Z.; Tian, Y.; Yang, D. Highly sensitive and fast-response hydrogen sensing of WO<sub>3</sub> nanoparticles via palladium reined spillover effect. *Nanoscale* **2021**, *13*, 12669–12675. [[CrossRef](#)] [[PubMed](#)]
16. Lee, J.; Jung, Y.; Sung, S.-H.; Lee, G.; Kim, J.; Seong, J.; Shim, Y.-S.; Jun, S.C.; Jeon, S. High-performance gas sensor array for indoor air quality monitoring: The role of Au nanoparticles on WO<sub>3</sub>, SnO<sub>2</sub>, and NiO-based gas sensors. *J. Mater. Chem. A* **2021**, *9*, 1159–1167. [[CrossRef](#)]
17. Ma, J.; Li, Y.; Zhou, X.; Yang, X.; Alharthi, F.A.; Alghamdi, A.A.; Cheng, X.; Deng, Y. Au nanoparticles decorated mesoporous SiO<sub>2</sub>-WO<sub>3</sub> hybrid materials with improved pore connectivity for ultratrace ethanol detection at low operating temperature. *Small* **2020**, *16*, 2004772. [[CrossRef](#)] [[PubMed](#)]
18. Yang, S.; Sun, J.; Xu, L.; Zhou, Q.Q.; Chen, X.F.; Zhu, S.D.; Dong, B.; Lu, G.Y.; Song, H.W. Au@ZnO functionalized three-dimensional macroporous WO<sub>3</sub>: A application of selective H<sub>2</sub>S gas sensor for exhaled breath biomarker detection. *Sens. Actuators B Chem.* **2020**, *324*, 128725. [[CrossRef](#)]
19. Tammanoon, N.; Iwamoto, T.; Ueda, T.; Hyodo, A.; Wisitsoraat, C.; Liwhiran, Y.; Shimizu, Y. Synergistic effects of PdOx-CuOx loadings on methyl mercaptan sensing of porous WO<sub>3</sub> microspheres prepared by ultrasonic spray pyrolysis. *ACS Appl. Mater. Interfaces* **2020**, *12*, 41728–41739. [[CrossRef](#)]
20. Gao, X.; Liu, H.; Wang, T.; Jiang, Z.; Zhu, Y. Low temperature preservation for perishable ready to eat foods: Not entirely effective for control of *L. monocytogenes*. *Trends Food Sci. Technol.* **2023**, *124*, 104228. [[CrossRef](#)]
21. Listeriosis. Available online: <https://www.who.int/news-room/fact-sheets/detail/listeriosis> (accessed on 7 April 2024).
22. Zhu, Z.; Zheng, L.; Zheng, S.; Chen, J.; Liang, M.; Tian, Y.; Yang, D. Cr doped WO<sub>3</sub> nanofibers enriched with surface oxygen vacancies for highly sensitive detection of the 3-hydroxy-2-butanone biomarker. *J. Mater. Chem. A* **2018**, *6*, 21419. [[CrossRef](#)]
23. Pereira, E.; Conrad, A.; Tesfai, A.; Palacios, A.; Kandari, R.; Kearney, A.; Locas, A.; Jamieson, F.; Elliot, E.; Otto, M.; et al. Multinational outbreak of *Listeria monocytogenes* infections linked to enoki mushrooms imported from the Republic of Korea 2016–2020. *J. Food Protect.* **2023**, *86*, 100101. [[CrossRef](#)] [[PubMed](#)]
24. Liu, A.; Shen, L.; Zeng, Z.; Sun, M.; Liu, Y.; Liu, S.; Li, C.; Wang, X. A minireview of the methods for *Listeria monocytogenes* detection. *Food Anal. Methods* **2018**, *11*, 215–223. [[CrossRef](#)]
25. Wang, Y.; Li, Y.; Yang, J.; Ruan, J.; Sun, C. Microbial volatile organic compounds and their application in microorganism identification in foodstuff. *TrAC Trend Anal. Chem.* **2016**, *78*, 1–16. [[CrossRef](#)]
26. Zhu, Y.; Zhao, Y.; Ma, J.; Cheng, X.; Xie, J.; Xu, P.; Liu, H.; Liu, H.; Zhang, H.; Wu, M.; et al. Mesoporous tungsten oxides with crystalline framework for highly sensitive and selective detection of foodborne pathogens. *J. Am. Chem. Soc.* **2017**, *139*, 10365–10373. [[CrossRef](#)]
27. Ma, J.H.; Li, Y.Y.; Li, J.C.; Yang, X.; Ren, Y.; Alghamdi, A.A.; Song, G.; Yuan, K.; Deng, Y. Rationally designed dual-mesoporous transition metal oxides/noble metal nanocomposites for fabrication of gas sensors in real-time detection of 3-Hydroxy-2-butanone biomarker. *Adv. Funct. Mater.* **2021**, *32*, 2107439. [[CrossRef](#)]
28. Zeb, S.; Cui, Y.; Zhao, H.; Sui, Y.; Yang, Z.; Khan, Z.U.; Ahmad, S.M.; Ikram, M.; Gao, Y.; Jiang, X. Synergistic effect of Au-PdO modified Cu-doped K<sub>2</sub>W<sub>4</sub>O<sub>13</sub> nanowires for dual selectivity high performance gas sensing. *ACS Appl. Mater. Interfaces* **2022**, *14*, 13836–13847. [[CrossRef](#)]
29. Wang, C.; Du, L.; Xing, X.; Feng, D.; Tian, Y.; Li, Z.; Zhao, X.; Yang, D. Radial ZnO nanorods decorating Co<sub>3</sub>O<sub>4</sub> nanoparticles for highly selective and sensitive detection of the 3-hydroxy-2-butanone biomarker. *Nanoscale* **2022**, *14*, 482–491. [[CrossRef](#)] [[PubMed](#)]
30. Zhao, H.; Mao, Q.; Jian, L.; Dong, Y.; Zhu, Y. Photodeposition of earth-abundant cocatalysts in photocatalytic water splitting: Methods, functions, and mechanisms. *Chin. J. Catal.* **2022**, *43*, 1774–1804. [[CrossRef](#)]
31. Fernando, J.F.; Shortell, M.P.; Noble, C.J.; Harmer, J.R.; Jaatinen, E.A.; Waclawik, E.R. Controlling Au photodeposition on large ZnO nanoparticles. *ACS Appl. Mater. Interfaces* **2016**, *8*, 14271–14283. [[CrossRef](#)]
32. Bai, S.L.; Li, D.Q.; Han, D.M.; Luo, R.; Chen, A.; Chung, C.L. Preparation, characterization of WO<sub>3</sub>-SnO<sub>2</sub> nanocomposites and their sensing properties for NO<sub>2</sub>. *Sens. Actuators B Chem.* **2010**, *150*, 749–755. [[CrossRef](#)]
33. Cao, P.J.; Huang, Q.G.; Navale, S.T.; Fang, M.; Liu, X.K.; Zeng, Y.X.; Liu, W.J.; Stadler, F.J.; Lu, Y.M. Integration of mesoporous ZnO and Au@ZnO nanospheres into sensing device for the ultrasensitive CH<sub>3</sub>COCH<sub>3</sub> detection down to ppb levels. *Appl. Surf. Sci.* **2020**, *518*, 146223. [[CrossRef](#)]
34. Song, X.P.; Xu, Q.; Zhang, T.; Song, B.; Li, C.; Cao, B. Room-temperature, high selectivity and low-ppm-level triethylamine sensor assembled with Au decahedrons-decorated porous α-Fe<sub>2</sub>O<sub>3</sub> nanorods directly grown on flat substrate. *Sens. Actuators B Chem.* **2018**, *268*, 170–181. [[CrossRef](#)]

35. Wang, D.; Tian, L.; Li, H.J.; Wan, K.; Yu, X.; Wang, P.; Chen, A.; Wang, X.; Yang, J. Mesoporous ultrathin SnO<sub>2</sub> nanosheets in situ modified by graphene oxide for extraordinary formaldehyde detection at low temperatures. *ACS Appl. Mater. Interfaces* **2019**, *11*, 12808–12818. [[CrossRef](#)] [[PubMed](#)]
36. Ma, J.H.; Ren, Y.A.; Zhou, X.R.; Liu, L.; Zhu, Y.; Cheng, X.; Xu, P.; Li, X.; Deng, Y.; Zhao, D. Pt nanoparticles sensitized ordered mesoporous WO<sub>3</sub> semiconductor: Gas sensing performance and mechanism study. *Adv. Funct. Mater.* **2017**, *28*, 1705268. [[CrossRef](#)]
37. Nayak, A.K.; Ghosh, R.; Santra, S.; Guha, P.K.; Pradhan, D. Hierarchical nanostructured WO<sub>3</sub>-SnO<sub>2</sub> for selective sensing of volatile organic compounds. *Nanoscale* **2015**, *7*, 12460–12473. [[CrossRef](#)] [[PubMed](#)]
38. Wei, Z.; Wang, W.; Li, W.; Bai, X.; Zhao, J.; Tse, E.C.M.; Phillips, D.L.; Zhu, Y. Steering electron-hole migration pathways using oxygen vacancies in tungsten oxides to enhance their photocatalytic oxygen evolution performance. *Angew. Chem. Int. Ed.* **2021**, *60*, 8236–8242. [[CrossRef](#)] [[PubMed](#)]
39. Xu, D.; Ge, K.; Qi, S.; Chen, Y.; Qiu, J.; Liu, Q. Hydrangea-like mesoporous WO<sub>3</sub> nanoflowers with crystalline framework for 3-hydroxy-2-butanone sensing. *Anal. Bioanal. Chem.* **2020**, *412*, 8371–8378. [[CrossRef](#)] [[PubMed](#)]
40. Chen, J.; Zhu, Z.Y.; Zheng, S.Z.; Du, L.; Xing, X.; Feng, D.; Li, S.; Yang, D. Synthesis of zinc oxide-alumina nanocables for detection of 3-hydroxy-2-butanone biomarker. *Mater. Lett.* **2019**, *253*, 121–123. [[CrossRef](#)]
41. Jiang, Z.Q.; Wang, C.; Yang, Z.L.; Jin, J. Highly sensitive 3-hydroxy-2-butanone gas sensor based on p-Cr<sub>2</sub>O<sub>3</sub>/n-SnO<sub>2</sub> binary heterojunction nanofibers. *Mater. Lett.* **2022**, *325*, 132856. [[CrossRef](#)]
42. Cai, H.J.; Liu, H.Q.; Ni, T.J.; Pan, Y.; Zhao, Y.; Zhu, Y. Controlled synthesis of Pt doped SnO<sub>2</sub> mesoporous hollow nanospheres for highly selective and rapidly detection of 3-Hydroxy-2-Butanone biomarker. *Front. Chem.* **2019**, *7*, 843. [[CrossRef](#)] [[PubMed](#)]
43. Chen, J.; Feng, D.L.; Wang, C.; Xing, X.; Du, L.; Zhu, Z.; Huang, X.; Yang, D. Gas sensor detecting 3-Hydroxy-2-butanone biomarkers: Boosted response via decorating Pd nanoparticles onto the 010 facets of BiVO<sub>4</sub> decahedrons. *ACS Sens.* **2020**, *5*, 2620–2627. [[CrossRef](#)] [[PubMed](#)]
44. Zhu, Z.; Zheng, L.; Zheng, S.; Chen, J.; Xing, X.; Feng, D.; Yang, D. Multichannel pathway-enriched mesoporous NiO nanocuboids for the highly sensitive and selective detection of 3-hydroxy-2-butanone biomarkers. *J. Mater. Chem. A* **2019**, *7*, 10456–10463. [[CrossRef](#)]
45. Li, F.; Gao, X.; Wang, R.; Zhang, T. Design of WO<sub>3</sub>-SnO<sub>2</sub> core-shell nanofibers and their enhanced gas sensing performance based on different work function. *Appl. Surf. Sci.* **2018**, *442*, 30–37. [[CrossRef](#)]
46. Chen, K.; Xie, W.; Deng, Y.; Han, J.; Zhu, Y.; Sun, J.; Yuan, K.; Wu, L.; Deng, Y. Alkaloid precipitant reaction inspired controllable synthesis of mesoporous tungsten oxide spheres for biomarker sensing. *ACS Nano* **2023**, *17*, 15763–15775. [[CrossRef](#)]

**Disclaimer/Publisher's Note:** The statements, opinions and data contained in all publications are solely those of the individual author(s) and contributor(s) and not of MDPI and/or the editor(s). MDPI and/or the editor(s) disclaim responsibility for any injury to people or property resulting from any ideas, methods, instructions or products referred to in the content.